Dynamical Instability Produces Transform Faults at Mid-Ocean Ridges

Taras Gerya, *et al.*

Science **329**, 1047 (2010);
DOI: 10.1126/science.1191349

framework to explain the phenomenological success of the MFL description.

References and Notes

1. J. M. Maldacena, *Adv. Theor. Math. Phys.* **2**, 231 (1998).
2. S. S. Gubser, I. R. Klebanov, A. M. Polyakov, *Phys. Lett. B* **428**, 105 (1998).
3. E. Witten, *Adv. Theor. Math. Phys.* **2**, 505 (1998).
4. S. W. Hawking, *Commun. Math. Phys.* **43**, 199 (1975); erratum, **46**, 206 (1976).
5. J. D. Bekenstein, *Phys. Rev. D* **7**, 2333 (1973).
6. S. S. Gubser, I. R. Klebanov, A. W. Peet, *Phys. Rev. D* **54**, 3915 (1996).
7. P. K. Kovtun, D. T. Son, A. O. Starinets, *Phys. Rev. Lett.* **94**, 111601 (2005).
8. S. S. Lee, *Phys. Rev. D* **79**, 086006 (2009).
9. H. Liu, J. McGreevy, D. Vegh, http://arXiv.org/abs/0903.2477.
10. M. Cubrovic, J. Zaanen, K. Schalm, *Science* **325**, 439 (2009).
11. T. Faulkner, H. Liu, J. McGreevy, D. Vegh, http://arXiv.org/abs/0907.2694.
12. C. M. Varma, P. B. Littlewood, S. Schmitt-Rink, E. Abrahams, A. E. Ruckenstein, *Phys. Rev. Lett.* **63**, 1996 (1989).
13. P. W. Anderson, *Phys. Rev. Lett.* **64**, 1839 (1990).
14. G. Aeppli, T. E. Mason, S. M. Hayden, H. A. Mook, J. Kulda, *Science* **278**, 1432 (1997).
15. T. Valla *et al*., *Science* **285**, 2110 (1999).
16. J. L. Tallon *et al*., *Phys. Status Solidi* **215**, 531 (1999).
17. D. van der Marel *et al*., *Nature* **425**, 271 (2003).
18. C. Varma, *Phys. Rev. B* **55**, 14554 (1997).
19. P. Gegenwart, Q. Si, F. Steglich, *Nat. Phys.* **4**, 186 (2008).
20. A microscopic model that produces this critical fluctuation spectrum has been proposed recently in (*41, 42*).
21. A. Chamblin, R. Emparan, C. V. Johnson, R. C. Myers, *Phys. Rev. D* **60**, 064018 (1999).
22. Because we are working with a theory that is scale-invariant in the vacuum, all dimensional quantities can be expressed in units of the chemical potential μ. Throughout the paper, in order not to clutter equations, we often do not write factors of μ explicitly, which can be reinstated on dimensional ground.
23. T. Senthil, *Phys. Rev. B* **78**, 035103 (2008).
24. For marginal Fermi liquids proposed in (*12*), $d_1/\tilde{c}_1$ is equal to $-\pi/2$, for which case there is a particle-hole symmetry; that is, $\Sigma_2(-\omega) = \Sigma_2(\omega)$. In Eq. 5, this happens only for $q = 0$. The particle-hole asymmetry in our case for generic q can be attributed to the fact that quantum-critical fluctuations are charged. In our case, Eq. 5 receives analytic corrections in k in both exponent and prefactors.
25. E. Abrahams, C. M. Varma, *Proc. Natl. Acad. Sci. U.S.A.* **97**, 5714 (2000).
26. For the explicit form of g_1, see eq. S.10 in the supporting online material (SOM). For the $\nu_{k_F} = 1/2$ case there are additional logarithms; see eq. S.18.
27. S. A. Hartnoll, P. K. Kovtun, M. Muller, S. Sachdev, *Phys. Rev. B* **76**, 144502 (2007).
28. The optical conductivity should also contain a piece proportional to $\delta(\omega)$ at the $O(N^0)$ level, which can be interpreted as a correction to the corresponding $O(N^2)$ piece. The contribution from the Fermi surface does not give rise to a delta function at any nonzero temperature.
29. For its explicit form, see the discussion around eq. S.22 in the SOM.
30. G. R. Stewart, *Rev. Mod. Phys.* **73**, 797 (2001).
31. A. Shekhter, C. M. Varma, *Phys. Rev. B* **79**, 045117 (2009).
32. For a recent discussion and references, see (*43*).
33. P. A. Lee, N. Nagaosa, *Phys. Rev. B* **46**, 5621 (1992).
34. S. A. Hartnoll, J. Polchinski, E. Silverstein, D. Tong, *J. High Energy Phys.* **2010**, 120 (2010).
35. There is, however, a range of bulk parameters m,q where this back-reaction effect near the horizon appears not to arise (*34*).
36. T. Faulkner, J. Polchinski, http://arXiv.org/abs/1001.5049.
37. For a review and refences, see (*44*).
38. F. Denef, S. A. Hartnoll, http://arXiv.org/abs/0901.1160.
39. J. Zaanen, *Nature* **462**, 15 (2009).
40. T. Faulkner, G. T. Horowitz, J. McGreevy, M. M. Roberts, D. Vegh, *J. High Energy Phys.* **2010**, 121 (2010).
41. V. Aji, C. M. Varma, *Phys. Rev. Lett.* **99**, 067003 (2007).
42. V. Aji, C. M. Varma, *Phys. Rev. B* **79**, 184501 (2009).
43. S. S. Lee, *Phys. Rev. B* **80**, 165102 (2009).
44. G. T. Horowitz, http://arXiv.org/abs/1002.1722.

44. We thank E. Abrahams, P. Coleman, S. Hartnoll, G. Horowitz, S. Kachru, P. Lee, S.-S. Lee, J. Maldacena, J. Polchinski, K. Rajagopal, S. Sachdev, K. Schalm, E. Silverstein, S. Trivedi, C. M. Varma, J. Zaanen, and in particular T. Senthil for discussions and encouragement. This work was supported in part by funds provided by the U.S. Department of Energy (DOE) under cooperative research agreement DE-FG0205ER41360 and the Outstanding Junior Investigator program, and in part by an Alfred P. Sloan fellowship. Also supported in part by by NSF under grant no. NSF PHY05-51164 and the University of California, Santa Barbara Department of Physics.

Supporting Online Material

www.sciencemag.org/cgi/content/full/science.1189134/DC1
SOM Text
Figs. S1 to S4
References

4 March 2010; accepted 21 July 2010
Published online 5 August 2010;
10.1126/science.1189134
Include this information when citing this paper.

Dynamical Instability Produces Transform Faults at Mid-Ocean Ridges

Taras Gerya

Transform faults at mid-ocean ridges—one of the most striking, yet enigmatic features of terrestrial plate tectonics—are considered to be the inherited product of preexisting fault structures. Ridge offsets along these faults therefore should remain constant with time. Here, numerical models suggest that transform faults are actively developing and result from dynamical instability of constructive plate boundaries, irrespective of previous structure. Boundary instability from asymmetric plate growth can spontaneously start in alternate directions along successive ridge sections; the resultant curved ridges become transform faults within a few million years. Fracture-related rheological weakening stabilizes ridge-parallel detachment faults. Offsets along the transform faults change continuously with time by asymmetric plate growth and discontinuously by ridge jumps.

Mid-ocean ridges sectioned by transform faults are prominent surface expressions of terrestrial plate tectonics and contribute to the overall structure of constructive plate boundaries where new oceanic crust forms [e.g., (*1*–*8*)]. Ridge transform fault patterns and their stability depend on a wide range of physical parameters [e.g., divergence rate (*1*, *7*, *8*), thermal and extensional stresses (*2*, *3*), and pre-existing structures (*9*)], but the physical mechanisms controlling spontaneous nucleation and growth (*1*, *4*) of transform faults remain ambiguous. The geometric correspondence between passive margins and mid-ocean ridges suggests that transform fault patterns result from preexisting structures. It is, therefore, commonly viewed that transform faults develop in regions adjacent to offset ridge segments and that these offsets remain constant through time [e.g., (*1*–*3*)]. However, four lines of evidence from both analog models and nature contradict this common view (*4*, *10*), namely: (i) single straight ridges can develop into an orthogonal pattern (*1*, *11*–*13*), (ii) zero offset fracture zones exist (*5*, *14*), (iii) there is a relation between ridge segment length and spreading rate (*15*), and (iv) transform faults are not inherited from transverse rift structures and nucleate while or after spreading starts (*10*).

Numerical models of transform faults are relatively rare (*2*, *3*, *16*–*18*) because of the intrinsic three-dimensionality of the problem, which only recently became treatable with large-scale computing power. In contrast to freezing wax experiments in which pronounced orthogonal ridge transform fault patterns formed during large plate divergence and growth (*1*, *19*–*21*), previous numerical models focused on short-term processes such as stress and displacement distributions (*16*–*18*) and fault patterns that arise from various thermomechanical loads on plates with predefined ridge offsets (*2*, *3*). These numerical experiments are consistent with analog modeling in that transform faults should be rheologically very weak (*17*); they also delineated conditions under which various fault patterns can nucleate from initially existing plate structure perturbations (*2*, *3*). However, strain reached in these experiments was too small to test the long-term stability of transform faults and investigate their spontaneous nucleation and growth at unsegmented, straight ridges in a self-consistent manner.

This work documents results from high-resolution three-dimensional (3D) thermomechanical numerical models of the long-term plate spreading to investigate the physical conditions for the emergence of orthogonal ridge transform fault patterns (fig. S1). In contrast to previous numerical studies, our Eulerian-Lagrangian model (*22*) can model large strains, which is essential to

Swiss Federal Institute of Technology Zurich, Department of Geosciences, Zurich, Switzerland. E-mail: taras.gerya@erdw.ethz.ch

understand natural processes at divergent, constructive plate boundaries. The modeled spreading rates range from 1.9 to 7.6 cm/year (0.95 to 3.8 cm/year half rates) which simulates (ultra)slow to intermediate spreading ridges (*7*, *23*). Ridge geometries obtained in numerical experiments depend on model parameters (table S2, Figs. 1 to 4, and figs. S2 to S6) and combine several tectonic elements such as straight and curved ridges with hooked ridge tips, normal and detachment faults, ridge-orthogonal and oblique transform faults, intratransform spreading centers, and rotating blocks (microplates). The development of ridge-orthogonal transform faults from a single straight ridge was persistently replicated in numerical experiments.

At the initial stages of plate boundary evolution, the straight boundary is composed of two symmetrical conjugate normal faults along which deformation spontaneously localizes. After 1 million years, the plate boundary becomes gently curved in response to asymmetric plate growth that develops in alternate directions along successive ridge sections (Fig. 1A). Displacement along the dominant conjugate fault locally controls the asymmetric accretion of new lithosphere to the plates. The corresponding fault section gradually turns into a typical, upward convex detachment fault plane (Fig. 1B). Such ridge-parallel detachment faults and asymmetric plate growth exist in relatively slow spreading ridges (*6*, *24*–*26*). Fracture-related weakening, implemented as a brittle/plastic strain weakening in the models, breaks the symmetry by partitioning extensional displacements between the two conjugate faults, as shown in previous 2D numerical experiments on lithospheric extension (*27*) and shortening (*28*). The ridge curvature enhances with time in a self-accelerating manner (Figs. 1 and 2), leading to the emergence of transform faults along rotated ridge segments that became subparallel to the extension direction (Fig. 1, B and C). Transform faults are thus akin to rotated and stretched sections of the mid-ocean ridge. In this process, the proto-transform faults are the former detachment surfaces that gradually changed from normal to strike-slip faults (Fig. 1, B and C). The establishment of their vertical orientation occurs during the offset growth.

The dynamical instability from which transform faults originate has a rheological origin and can develop in the case of no gravity (Fig. 3A). The instability is comparable to extensional necking of a rigid layer in a soft surrounding [i.e., boudinage (*29*, *30*)] with the important difference that new material continuously adds to the stretched and rheologically strong lithospheric layer. The characteristic wavelength of the instability is related to the plate viscosity: 30 to 50 km in models with plate viscosity of 10^{22} Pa s (Figs. 1 and 3) and 10 to 20 km in models with lower plate viscosity of 10^{21} Pa s. Plate/asthenosphere viscosity contrast controls the attitude of transform faults: Larger viscosity contrast ($\geq 10^4$) favors vertical ridge-orthogonal faults, whereas smaller viscosity contrast ($\leq 10^3$) allows faults oblique to the ridge and dipping at shallower angles (table S1 and fig. S2, C and H). The brittle/plastic rheology of the growing plate is another important rheological control of the transform fault orientation: Vertical ridge-orthogonal faults develop faster and more frequently in experiments where wet tensile fracture condition (*22*) is applied. Both spreading rate and thermal conductivity of rocks notably affect the thermal structure of the plates and hence the transform fault nucleation processes (table S1). An increase in the spreading rate has the same effect as a decrease in the thermal conductivity: It causes thinning of the plate boundary, facilitates symmetric plate growth, and weakens the dynamical ridge instability (fig. S2A).

Nucleation of transform faults strongly depends on the ridge orientation relative to the plate motion: A deviation of this orientation by 11 to 27° from perpendicular to spreading direction enhances the development of transform faults (figs.

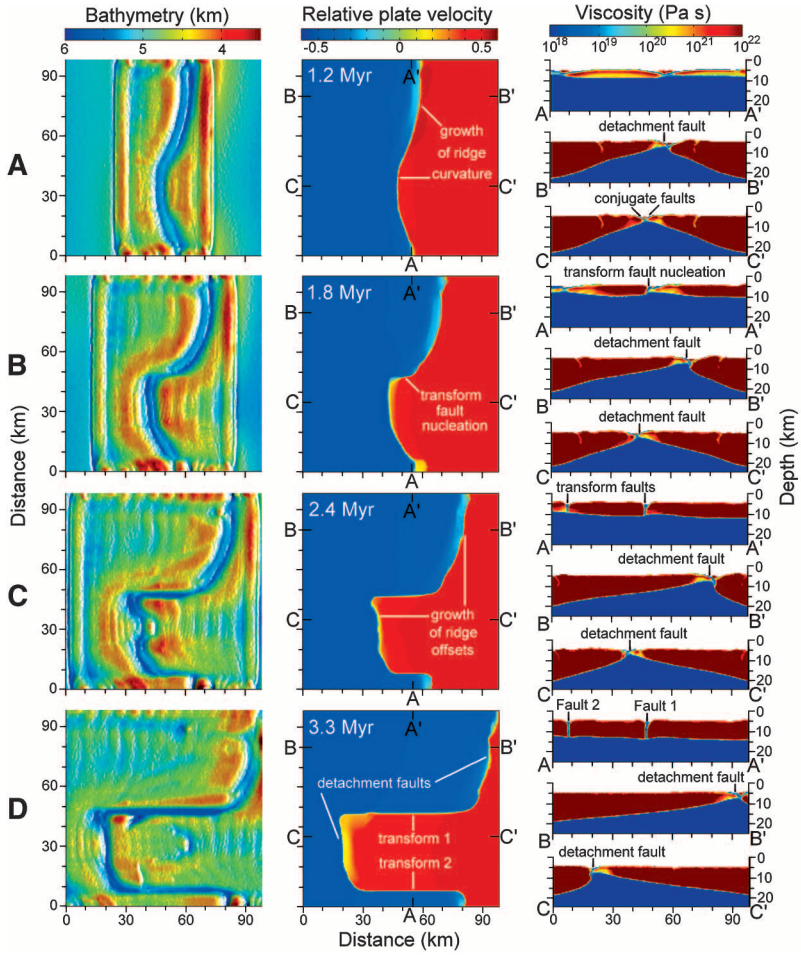

Fig. 1. Typical evolution of a constructive plate boundary with the emergence of transform faults (stages **A** to **D**). Numerical model parameters (*22*): spreading rate 3.8 cm/year, asthenospheric viscosity 10^{18} Pa s, plate viscosity 10^{22} Pa s, initial plate strength 30 MPa, final plate strength 3 MPa, strain weakening interval 0.2 to 1.2 (model named "dahzu" in table S1). Sea level for bathymetry maps (left column) corresponds to the top of the model. Horizontal velocity in the middle column is normalized to the spreading rate.

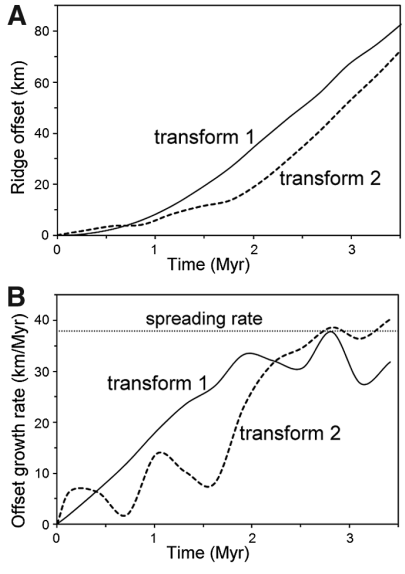

Fig. 2. Dependence of ridge offsets (**A**) and offset growth rates (**B**) versus time for two transform faults shown in Fig. 1.

S4 and S5). This suggests that after the transition from continental breakup to spreading (*10*), transform faults will grow faster from inclined ridge sections. The ensuing pattern will thus reflect to some degree an original large-scale curvature of the rifted margin. This might explain the geometric correspondence between passive margins and mid-ocean ridges. It also explains why transform faults develop rapidly at single straight ridges after a change in the spreading direction (*11*, *12*). Moreover, a similar instability may operate when changes in spreading direction generate extension across a pre-existing transform fault (*31*). In this case, the transform may behave as a ridge and rapidly breaks (*31*) into a series of shorter faults and intratransform spreading centers (*31*) (figs. S5B and S6C).

The growth of oceanic lithosphere by magmatic processes affects the geometry and the topography of mid-ocean ridges (*7*, *8*, *23*, *32*). Dynamic influences of this process were tested (table S1 and fig. S6) with a simple model that incorporates instantaneous melt extraction and deposition (*22*). Although crustal growth notably enhances ridge topography and results in a less-pronounced axial valley (*8*, *23*), the nucleation and development of transform faults is similar to models without magmatism (figs. S5 and S6). Continuous addition of nonfractured magmatic rocks to the surface of the plates dampens the asymmetry of plate accretion and delays growth of transform faults at the beginning of the experiments (figs. S5 and S6). At a later stage, a transition to more symmetric plate accretion and stabilization of transform fault offsets occurs (fig. S6, C and D).

Asymmetric plate growth does not change the relative plate rates across the transform faults (Figs. 1 and 3) because the rates of growth of two plates (A and B) separated by a ridge are partly independent of displacement rates of these plates with relations

$$v_{\mathrm{growth(A)}} + v_{\mathrm{growth(B)}} = v_{\mathrm{displacement(A)}} + v_{\mathrm{displacement(B)}} = v_{\mathrm{spreading}}$$

and

$$v_{\mathrm{ridge}} = [v_{\mathrm{displacement(A)}} - v_{\mathrm{growth(A)}}] = -[v_{\mathrm{displacement(B)}} - v_{\mathrm{growth(B)}}]$$

where $v_{\mathrm{growth(A)}}$ and $v_{\mathrm{growth(B)}}$ are growth rates of plates A and B, respectively, $v_{\mathrm{displacement(A)}}$ and $v_{\mathrm{displacement(B)}}$ are displacement rates of the same plates, $v_{\mathrm{spreading}}$ is the spreading rate, and v_{ridge} is the rate of ridge displacement [$v_{\mathrm{ridge}} = 0$ in the case of symmetric plate growth when $v_{\mathrm{displacement(A)}} = v_{\mathrm{growth(A)}}$ and thus $v_{\mathrm{displacement(B)}} = v_{\mathrm{growth(B)}}$].

The boundary instability is most efficient for the tested spreading rate of 3.8 to 5.7 cm/year (table S1). An 11 to 27° deviation of the initial ridge orientation from perpendicular to the spreading direction produces transform faults at 1.9 cm/year as well (table S1). Faster spreading rates of 7.6 cm/year cause thinning of the plate contact and preclude the development of stable detachment faults, with symmetric plate growth as a result (Fig. 3B and fig. S3). For slower extension rates of 1.9 cm/year, several parallel detachment faults develop simultaneously and preclude focusing deformation within a single boundary. In that case, transform faults are ill-defined and deformation is dominated by growth and rotation of multiple blocks (microplates) and ridge-parallel rolls (fig. S2B). This is consistent with the lack of transform faults in ultraslow spreading ridges (*7*). Numerical experiments thus suggest that transform faults may preferably grow within a certain range of slow to intermediate spreading rates and mark an intermediate stage of plate separation between initial slow rifting and later steady spreading. This was prominent in one numerical experiment where the initial spreading rate of 3.8 cm/year doubled after the appearance of transform faults (Fig. 3B). If

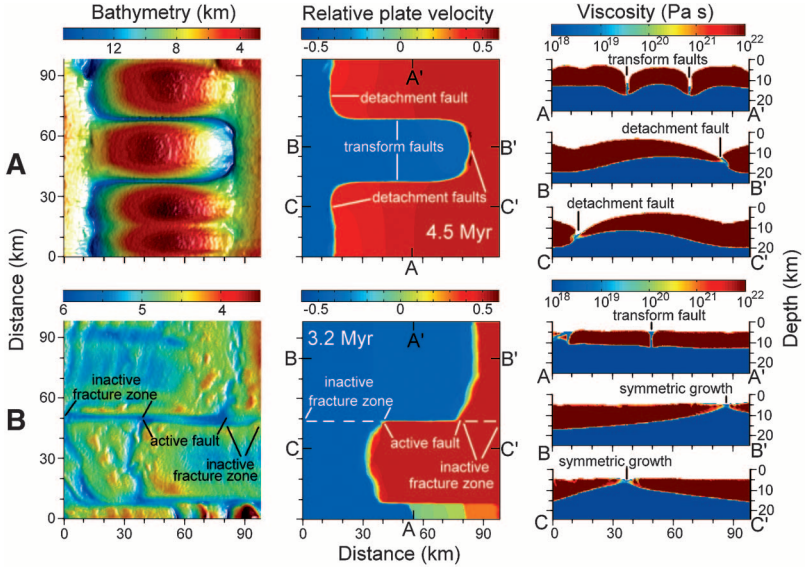

Fig. 3. Variations in model development for different parameters. Model parameters: (**A**) same as in Fig. 1 but without gravity results in larger model topographies, but does not preclude the formation of transform and detachment faults (model named "dahzi" in table S1); (**B**) same as in Fig. 1 but with a gradually increasing spreading rate from 3.8 to 7.6 cm/year within 2 to 2.5 million years after the beginning of the extension. Inactive fracture zones develop as a result of symmetric plate growth (model named "dahzg" in table S1).

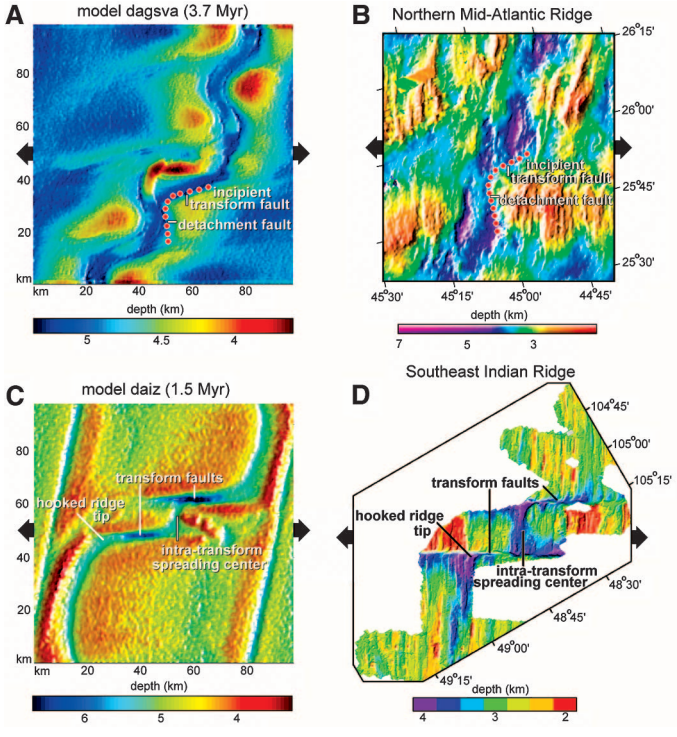

Fig. 4. Comparison of topography patterns developed in amagmatic (**A**) and magmatic (**C**) numerical models with bathymetry data for slow spreading Northern Mid-Atlantic Ridge (*11*) (**B**) and intermediate spreading Southeast Indian Ridge (*34*) (**D**). Model parameters for (A) and (C) are given in table S1.

the final spreading rate is high, symmetric growth will dominate, and offsets of ridge segments may stabilize (Fig. 3B). Stabilization of transform fault offsets with time may also be caused by magmatic processes (fig. S6) that are more intense at faster spreading rates (*7*, *8*, *23*, *32*). The range of spreading rates that favors nucleation and growth of transform faults by the dynamical instability depends on several model parameters, such as initial ridge orientation, thermal conductivity of rocks, plate viscosity, and intensity of magmatic processes. Tuning these parameters within the range of uncertainties for natural systems can provide better fit between nature and models. Also, transient asymmetric magmatic accretion processes indicated by magnetic data (*5*, *25*) may presumably cause transform faults nucleation and growth in magmatically dominated fast spreading ridges.

Spontaneous changes in the growth direction or symmetry of separated ridge segments produced inactive fracture zones in our experiments (Fig. 3B and fig. S3). The periodicity of such changes depends on the degree of strain weakening and is shorter for cases with the least weakening. Another mechanism changing ridge offsets is the formation of new detachment faults away from the ridge crest [i.e., ridge jumps (*6*)]. This process typically reduces the offsets (fig. S3) and may be a mechanical response to increasing stresses in the plate contact along transform faults.

Transform faults obtained in numerical experiments share similarities with natural observations. They are characterized by up to several km deep and wide topographic lows (*33*, *34*) (Figs. 1D, 3B, and 4). Ridge offsets along the faults vary from tens to 100 km (*15*, *34*) (Figs. 1, 3, and 4, and fig. S2). Development of the faults occurs on the time scale of plate separation and thus should react nearly instantaneously to changes in spreading direction (*11*, *12*) (figs. S4 to S6). Curved ridges generated in numerical experiments are similar to some of the natural ridge structures (Fig. 4). They have a pronounced, often asymmetric axial valley characteristic of slow to intermediate spreading ridges [spreading rates below 8 cm/year (*7*, *8*, *23*, *34*)]. Intratransform spreading centers and hooked ridge tips (Fig. 4, C and D, and figs. S5 and S6) are common in nature (*34*). Nucleation and growth of transform faults in numerical models are associated with detachment faults and asymmetric accretion (Fig. 1 and Fig. 4, A and B), which are well documented in nature based on seismic and bathymetric data (*6*, *24*, *26*). Asymmetric patterns of plate age distribution (figs. S4 to S6) and changes of ridge offsets with time (Figs. 1 and 2 and figs. S5 and S6) are indicated by magnetic data (*5*, *25*).

References and Notes

1. D. W. Oldenburg, J. N. Brune, *Science* **178**, 301 (1972).
2. C. F. Hieronymus, *Earth Planet. Sci. Lett.* **222**, 177 (2004).
3. E. Choi, L. Lavier, M. Gurnis, *Phys. Earth Planet. Inter.* **171**, 374 (2008).
4. D. Sandwell, *J. Geophys. Res.* **91** (B6), 6405 (1986).
5. P. R. Stoddard, S. Stein, *Mar. Geophys. Res.* **10**, 181 (1988).
6. K. M. Marks, J. M. Stock, *Mar. Geophys. Res.* **17**, 361 (1995).
7. H. J. B. Dick, J. Lin, H. Schouten, *Nature* **426**, 405 (2003).
8. C. Small, in *Faulting and Magmatism at Mid-Ocean Ridges*, W. R. Buck, P. T. Delaney, J. A. Karson, Y. Lagabrielle, Eds. (American Geophysical Union, Washington, DC, 1998), pp. 1–26.
9. T. Tentler, V. Acocella, *J. Geophys. Res.* **115** (B1), B01401 (2010).
10. B. Taylor, A. Goodliffe, F. Martinez, *C. R. Geosci.* **341**, 428 (2009).
11. H. W. Menard, T. Atwater, *Nature* **219**, 463 (1968).
12. S. A. Merkur'ev, C. DeMets, N. I. Gurevich, *Geotectonics* **43**, 194 (2009).
13. E. L. Winterer, in *The Geophysics of the Pacific Ocean Basin and Its Margin*, G. H. Sutton, M. H. Manghnani, R. Moberly, Eds. (American Geophysical Union, Washington, DC, 1976), pp. 269–280.
14. H. Schouten, R. S. White, *Geology* **8**, 175 (1980).
15. P. J. Fox, D. G. Gallo, *Tectonophys.* **104**, 205 (1984).
16. A. Gudmundsson, *Earth Planet. Sci. Lett.* **136**, 603 (1995).
17. M. D. Behn, J. Lin, M. T. Zuber, *Geophys. Res. Lett.* **29**, 2207 (2002).
18. A. Hashima, Y. Takada, Y. Fukahata, M. Matsuura, *Geophys. J. Int.* **175**, 992 (2008).
19. D. Oldenburg, J. Brune, *J. Geophys. Res.* **80**, 2575 (1975).
20. R. Ragnarsson, J. L. Ford, C. D. Santangelo, E. Bodenschatz, *Phys. Rev. Lett.* **76**, 3456 (1996).
21. R. F. Katz, R. Ragnarsson, E. Bodenschatz, *N. J. Phys.* **7**, 37 (2005).
22. Methods are available as supporting material on *Science* Online.
23. K. A. Kriner, R. A. Pockalny, R. L. Larson, *Earth Planet. Sci. Lett.* **242**, 98 (2006).
24. J. S. Collier, J. J. Danobeitia, CD82 Scientific Party, *Geology* **25**, 1075 (1997).
25. S. Allerton, J. Escartín, R. C. Searle, *Geology* **28**, 179 (2000).
26. J. Escartín *et al.*, *Nature* **455**, 790 (2008).
27. R. S. Huismans, C. Beaumont, *Geology* **30**, 211 (2002).
28. S. M. Schmalholz, B. J. P. Kaus, J.-P. Burg, *Geology* **37**, 775 (2009).
29. R. B. Smith, *Geol. Soc. Am. Bull.* **88**, 312 (1977).
30. W. R. Buck, L. L. Lavier, A. N. B. Poliakov, *Philos. Trans. R. Soc. London Ser. A* **357**, 671 (1999).
31. R. A. Pockalny, P. J. Fox, D. J. Fornari, K. C. Macdonald, M. R. Perfit, *J. Geophys. Res.* **102** (B2), 3167 (1997).
32. W. R. Buck, L. L. Lavier, A. N. B. Poliakov, *Nature* **434**, 719 (2005).
33. P. M. Gregg, J. Lin, M. D. Behn, L. G. J. Montési, *Nature* **448**, 183 (2007).
34. C. DeMets, R. G. Gordon, D. F. Argus, *Geophys. J. Int.* **181**, 1 (2010).

35. I thank Y. Podladchikov, J.-P. Burg, B. Kaus, P. Tackley, and three anonymous reviewers for suggestions and discussions. This work was supported by the TopoEurope and 4D-Adamello projects of Swiss National Science Foundation.

Supporting Online Material

www.sciencemag.org/cgi/content/full/329/5995/1047/DC1
Methods
Figs. S1 to S6
Table S1
References

23 April 2010; accepted 23 July 2010
10.1126/science.1191349

The Chlorine Isotope Composition of the Moon and Implications for an Anhydrous Mantle

Z. D. Sharp,[1]* C. K. Shearer,[1,2] K. D. McKeegan,[3] J. D. Barnes,[4] Y. Q. Wang[5]

Arguably, the most striking geochemical distinction between Earth and the Moon has been the virtual lack of water (hydrogen) in the latter. This conclusion was recently challenged on the basis of geochemical data from lunar materials that suggest that the Moon's water content might be far higher than previously believed. We measured the chlorine isotope composition of Apollo basalts and glasses and found that the range of isotopic values [from −1 to +24 per mil (‰) versus standard mean ocean chloride] is 25 times the range for Earth. The huge isotopic spread is explained by volatilization of metal halides during basalt eruption—a process that could only occur if the Moon had hydrogen concentrations lower than those of Earth by a factor of ~10^4 to 10^5, implying that the lunar interior is essentially anhydrous.

The origin of the Moon is constrained by geophysical models of angular momentum, density and mass, and geochemical arguments based on chemical and isotopic similarities and differences between Earth and the Moon. It is now generally accepted that the Moon was formed from the impact of a Mars-sized body sometime after formation of Earth's core (*1*, *2*), although a number of observations have not been adequately explained. Geodynamic models indicate that the impactor came from a different region of our solar system and that the bulk of the Moon originated from the impactor rather than Earth (*3*). This result is at odds with geochemical data, such as the fact that Earth and the Moon have identical oxygen and chromium isotope ratios (*4*, *5*). If the two bodies came from different regions of our solar system, it is expected that they would have different isotope ratios (*6*). Turbulent mixing between the molten Earth and the Moon immediately after impact has been proposed as a

[1]Department of Earth and Planetary Sciences, University of New Mexico, Albuquerque, NM 87122, USA. [2]Institute of Meteoritics, University of New Mexico, Albuquerque, NM 87122, USA. [3]Department of Earth and Space Sciences, University of California, Los Angeles, CA 90095, USA. [4]Department of Geological Sciences, University of Texas, Austin, TX 78712, USA. [5]Materials Science and Technology Division, Los Alamos National Laboratory, Los Alamos, NM 87545, USA.

*To whom correspondence should be addressed. E-mail: zsharp@unm.edu

www.sciencemag.org/cgi/content/full/329/5995/1047/DC1

Supporting Online Material for

Dynamical Instability Produces Transform Faults at Mid-Ocean Ridges

Taras Gerya

E-mail: taras.gerya@erdw.ethz.ch

Published 27 August 2010, *Science* **329**, 1047 (2010)
DOI: 10.1126/science.1191349

This PDF file includes:

Supporting online material for:

Dynamical instability produces transform faults at mid-ocean ridges

Gerya, T.

ETH-Zurich, Department of Geosciences, Zurich, Switzerland.

Corresponding author: T. Gerya (e-mail: taras.gerya@erdw.ethz.ch).

Methods

The employed numerical code I3ELVIS (*1*) combines conservative finite differences on a fully staggered grid and marker-in-cell techniques with multigrid solver and allows for large viscosity contrasts and strong localization of visco-plastic deformation (*2*). The Eulerian computational domain is equivalent to 98x98x34 km (Fig. S1) and is resolved with a regular rectangular grid of 197x197x69 nodes and contains 21 millions randomly distributed Lagrangian markers (models up to 196x196x34 km were also explored, see Table S1). The momentum, mass and heat conservation equations are solved on the non-deforming Eulerian grid whereas the advection of transport properties including viscosity, plastic strain, temperature etc. is performed with the moving Lagrangian markers. Lagrangian markers leave the Eulerian model domain through the left and right lateral boundaries and are then recycled through the top and the bottom of the model as sea water and mantle markers, respectively. This Eulerian-Lagrangian numerical modelling scheme with open boundaries allows for an infinitely long plate separation with the use of laterally limited Eulerian computational domain and relatively small amount of continuously recycled Lagrangian markers.

The thermal structure of the initial plate setup is computed according to the cooling of a semi-infinite, half-space (*3*):

$$T = T_1 + (T_0 - T_1)(1 - erf(\eta)),$$

$$\eta = \frac{d}{2\sqrt{\kappa\ \tau}},$$

where T_0 = 273 K C and T_1 = 1573 K is the surface and asthenospheric mantle temperature, respectively; κ is thermal diffusivity (10^{-6} m^2 s^{-1}), τ is the age in seconds of the plates and η is the dimensionless similarity variable as the function of depth d in meters below the plate surface. In order to insure an efficient heat transfer from the upper surface of the plate, thermal conductivity of the sea water layer above this plate (Fig. 1) is taken to be hundred times higher (200 W/m/K) than that of the plate (1-4 W/m/K).

The rheological model implies constant low viscosity (10^{18}-10^{20} Pa s) of the asthenospheric mantle (T>1300 K) and visco-plastic rheology of the lithospheric plates (T<1300 K) with temperature-independent background viscosity that is 2-5 orders of magnitude higher (10^{20}-10^{23} Pa s) than that of the asthenosphere. Compared to previous models of mid-ocean ridges (*4-6*), this rheological model does not account for power-law rheology and elasticity of the lithosphere and neglect thermally induced stresses. Brittle/plastic rheology of the plates assumes fracture-related strain weakening (*4,5*,*7*) and is implemented by using plate strength limitation in form

$$\sigma_{II} \le C_\gamma + \phi_P \left(P - P_f\right),$$

$\phi_P = 1$ when $P<P_f$ (tensile fracture), $\phi_P = 0$ when $P \ge P_f$ (confined fracture)

$P_f = \rho g y$ for wet fracture, $P_f = 0$ for dry fracture,

$C_\gamma = C_0$ when $\gamma \le \gamma_0$, $C_\gamma = C_0 + (\gamma - \gamma_0)\dfrac{C_1 - C_0}{\gamma_1 - \gamma_0}$ when $\gamma_0 < \gamma < \gamma_1$, $C_\gamma = C_1$ when $\gamma \ge \gamma_1$,

$$\gamma = \int \sqrt{\frac{1}{2}\left(\dot{\varepsilon}_{ij(plastic)}\right)^2}\, dt,$$

$$\sigma_{II} = \sqrt{\frac{1}{2}\left(\sigma'_{ij}\right)^2},$$

where σ_{II} is second stress invariant (Pa), P is dynamic pressure on solids (Pa), P_f is fluid pressure (Pa), y is vertical coordinate (m), g = 9.81 m/s^2 is gravitational acceleration, ρ_f = 1000 kg/m^3 is water density, γ is integrated plastic strain (γ_0 and γ_1 are the upper and lower strain limits for the fracture-related weakening, respectively), t is time (s), $\dot{\varepsilon}_{ij(plastic)}$ is plastic strain rate tensor, C_γ is the plate strength at P-P_f=0 (for both confined and tensile fracture) that depends on the plastic strain γ (C_0 and C_1 are the initial and final strength values for the fracture-related weakening, respectively). The stress limitation for tensile fracture is formulated from a theoretical criterion (*8*) for tensile failure of a fluid-filled crack. This criterion is based on Griffith's theory (*9*) and has been verified experimentally (*10*). Strain weakening assumed in the model is similar to those in previous numerical studies of mid-ocean ridges (*4*,*5*). It is related, in particular, to water and melt percolation along fault zones and their intense serpentinization that strongly decreases strength of fractured fault rocks (*7*,*11*,*12*).

Influences of an oceanic crust growth by melt extraction and deposition that affects ridge geometry and topography (*4*,*13*,*14*) was tested in a few experiments. The crustal growth algorithm (*15*) includes dry partial melting of the mantle and instantaneous melt extraction and transport producing crust deposition on the surface. The standard (i.e. without melt extraction) volumetric degree of mantle melting M_0 changes with pressure and temperature as,

$$M_0 = 0 \text{ when } T < T_{\text{solidus}},$$

$$M_0 = (T - T_{\text{solidus}}) / (T_{\text{liquidus}} - T_{\text{solidus}}) \text{ when } T_{\text{solidus}} < T < T_{\text{liquidus}},$$

$$M_0 = 1 \text{ when } T > T_{\text{liquidus}},$$

where $T_{\text{solidus}} = 1394 + 0.132899P - 0.000005104P^2$ and $T_{\text{liquidus}} = 2073 + 0.114P$ are, respectively, solidus and liquidus temperature (K) of the mantle (*16,17*) at a given pressure P (MPa). Markers tracked the amount of melt extracted during the evolution of

each experiment. The total amount of melt, M, for every marker takes into account the amount of previously extracted melt and is calculated as

$$M = M_0 - \Sigma_n M_{ext},$$

where $\Sigma_n M_{ext}$ is the total melt fraction extracted during the previous n extraction episodes. The rock is considered non-molten (refractory) when the extracted melt fraction is bigger than the standard one (i.e. when $\Sigma_n M_{ext} > M_0$). If the total amount of melt M for a given marker is > 0, the melt fraction $M_{ext} = M$ is extracted and $\Sigma_n M_{ext}$ is updated. The extracted melt fraction M_{ext} is assumed to propagate upward to the surface much faster than the plates deform (*18*). Hence, the instantaneous transmission of extracted melt to the growing crust is reasonable. At every time step, extracted melts are added on the plate surface and build up new non-fractured portions of the oceanic crust. This simple instantaneous melt extraction-deposition model does not discriminates between volcanic and plutonic (e.g. dyking) crust additions nor does it account for compaction and lateral transport of the melts in the mantle (*4*, *18*, *19*).

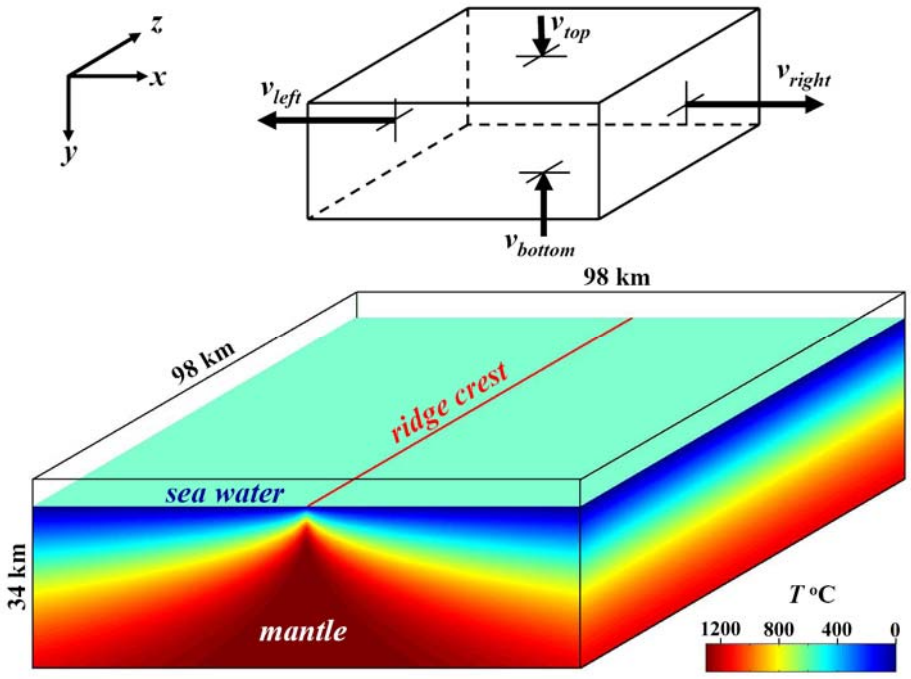

Figure S1. Initial model setup and boundary conditions for 3D thermomechanical numerical experiments. Boundary conditions are constant spreading rate in *x*-direction ($v_{spreading} = v_{left} + v_{right}$, where $v_{left} = v_{right}$) and compensating vertical influx velocities through the upper and lower boundaries (v_{top} and v_{bottom}) to ensure conservation of mass; front and back boundaries are free slip. A water-loaded free surface condition for the upper plate boundary is implemented by using a weak layer approach (*22*): the weak sea water layer is initially 5 km thick, has a characteristic density of 1000 kg/m^3 and a viscosity of 10^{18} Pa s to ensure small stresses (<10^5 Pa) along the upper plate interface. The symmetric initial thermal structure corresponds to a cooling age which linearly increases from 0.1 Myrs in the center of the model to 5 Myrs at the left and right boundaries. Thermal boundary conditions are insulating at all boundaries with except of the upper and lower boundaries at which constant temperature of 273 K and 1573 K is prescribed, respectively.

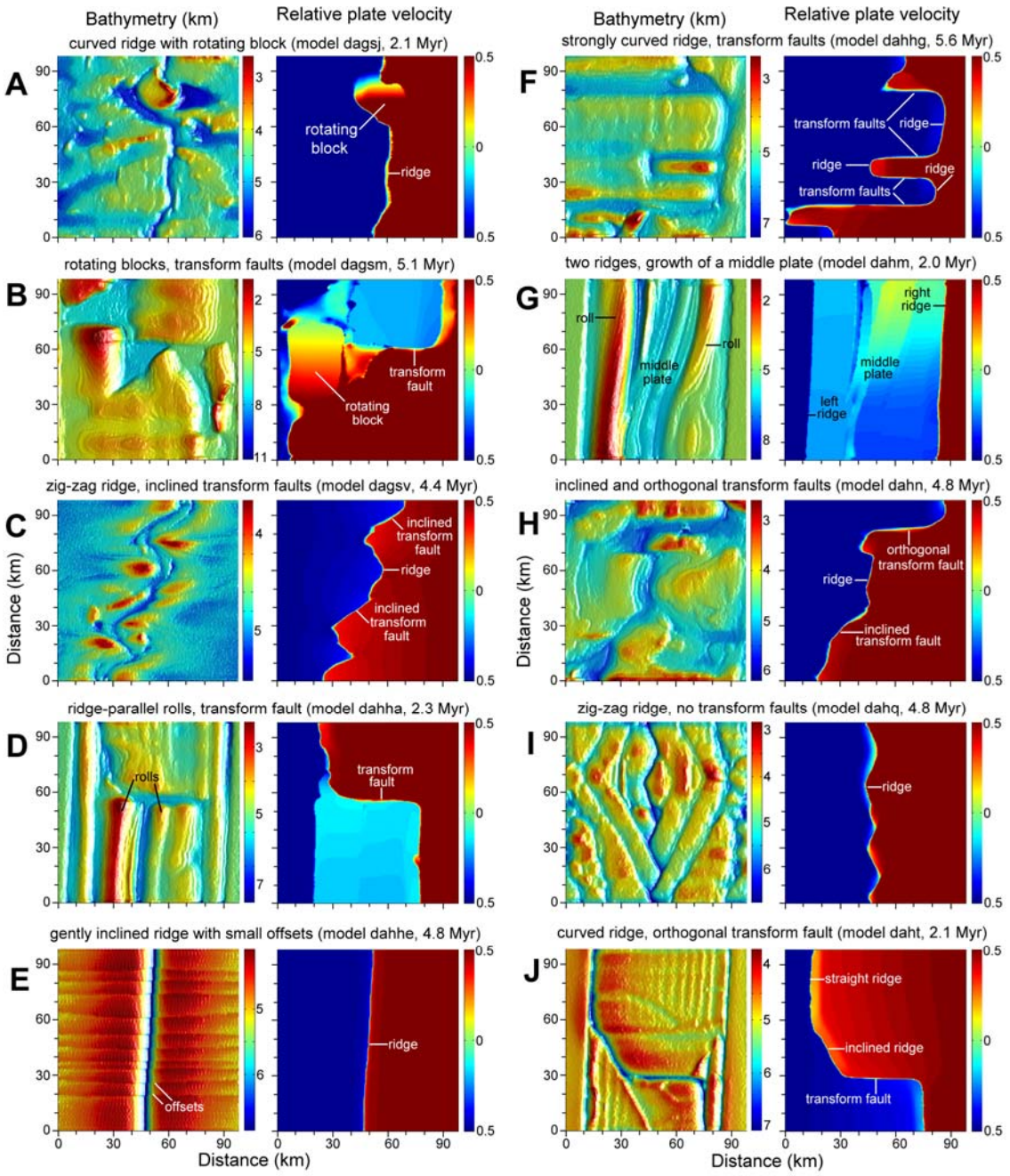

Figure S2. Representative ridge geometries obtained in numerical experiments. Model parameters are given in Table S1

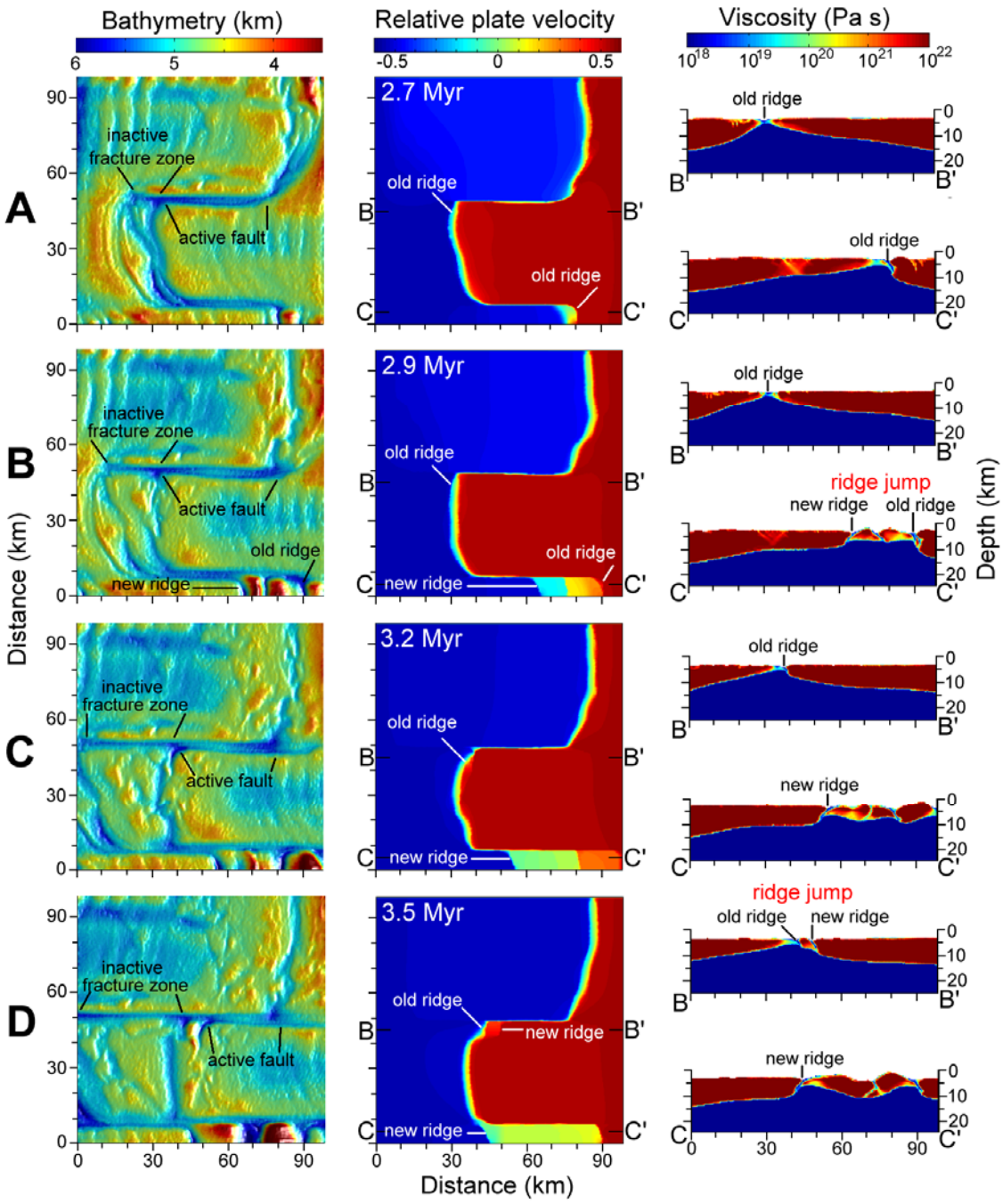

Figure S3. Development of ridge jumps and inactive fracture zones in the numerical experiment with increasing spreading rate (Model dahzg in Table S1).

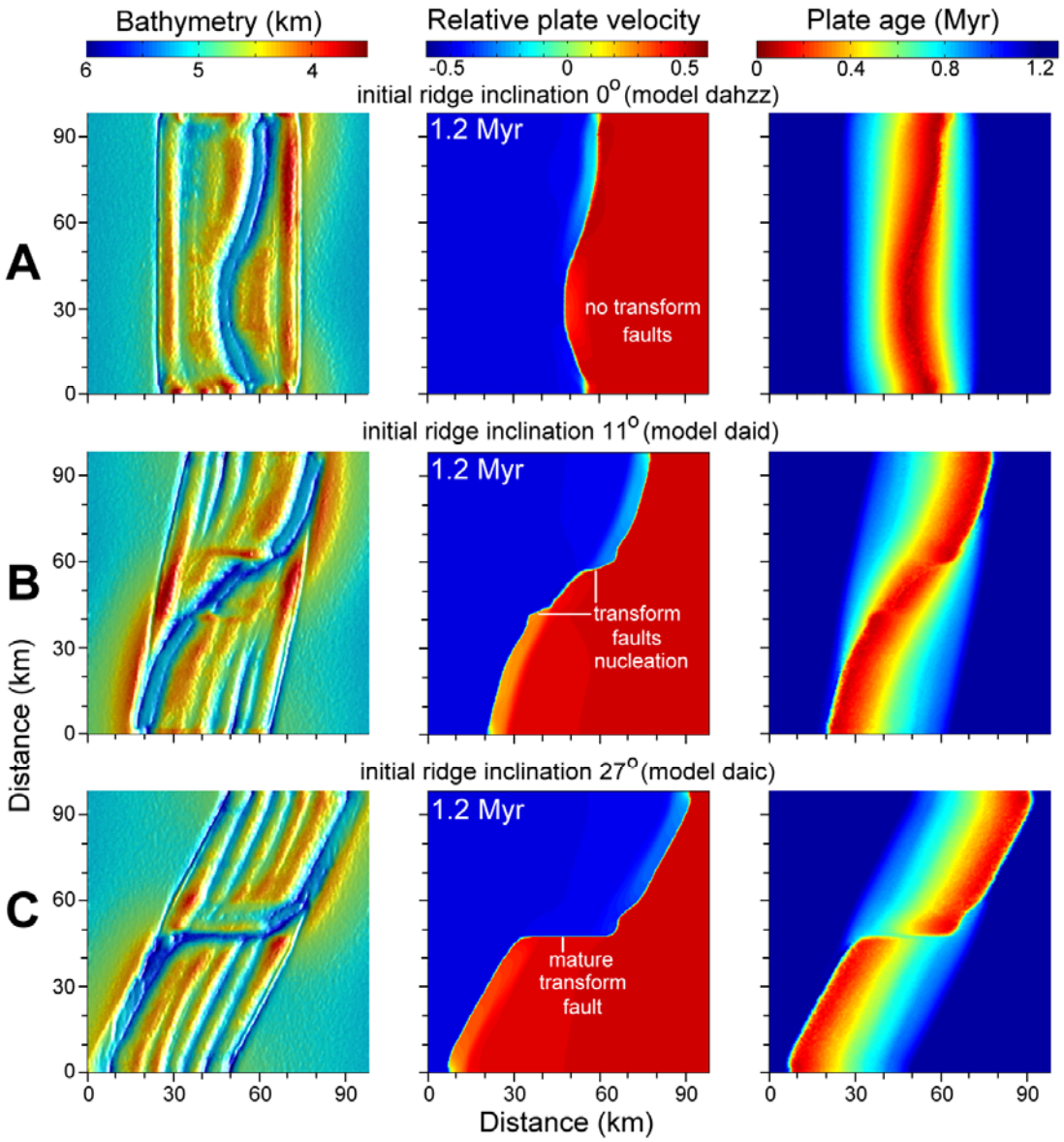

Figure S4. Influence of initial ridge inclination (to z axis) on the transform fault development. Plate age in the left column is computed for Lagrangian markers found at the plate surface as the age of their thermal accretion to the plate (i.e. age of cooling below 1300 K, see Methods). Note asymmetry of plate age patterns in (B) and (C) caused by asymmetric plate growth.

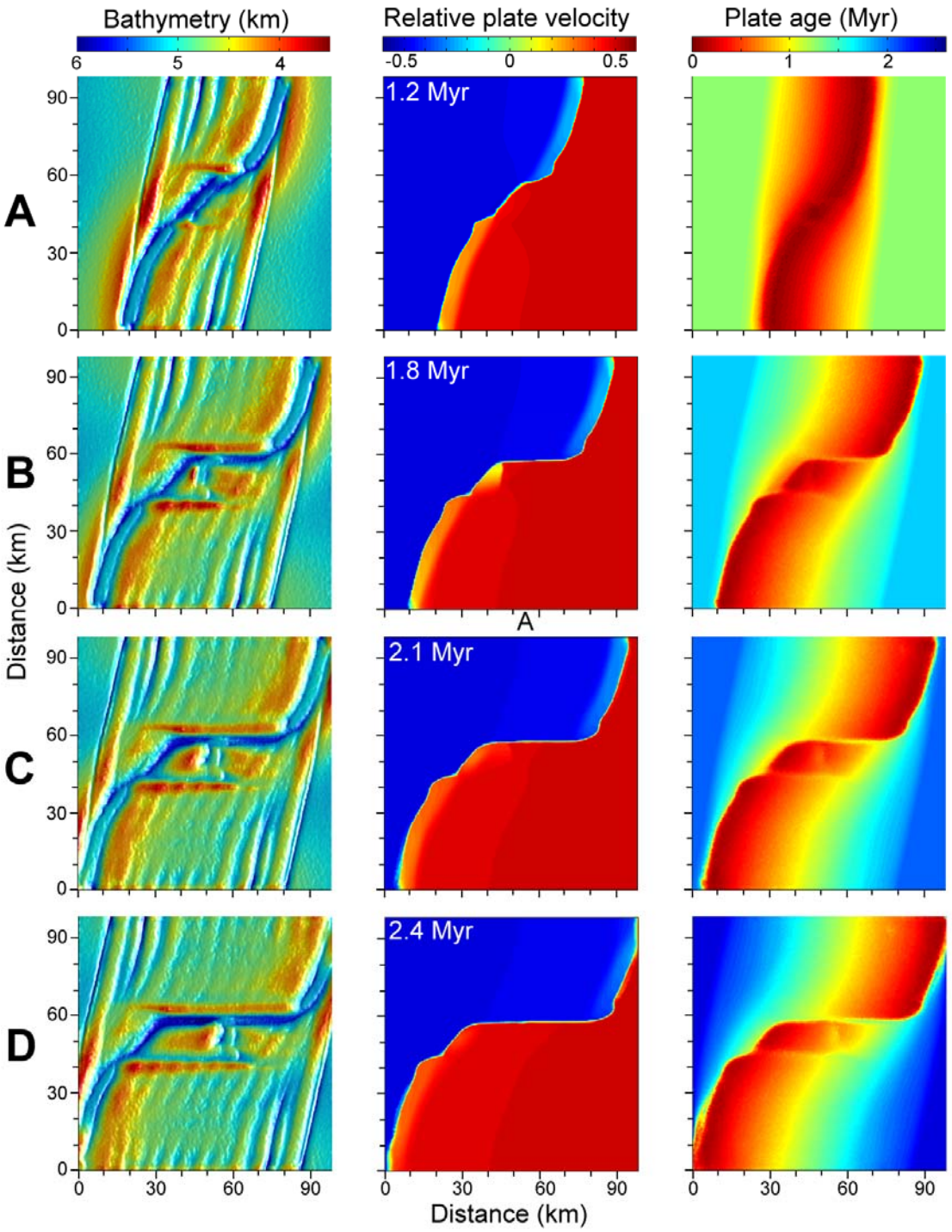

Figure S5. Development of transform faults for an initially inclined ridge (Model daid in Table S1, initial ridge inclination to z-axis is 11^{o}). Magmatic growth of the crust is not modeled. Note close parallel transform faults with the narrow intra-transform spreading center.

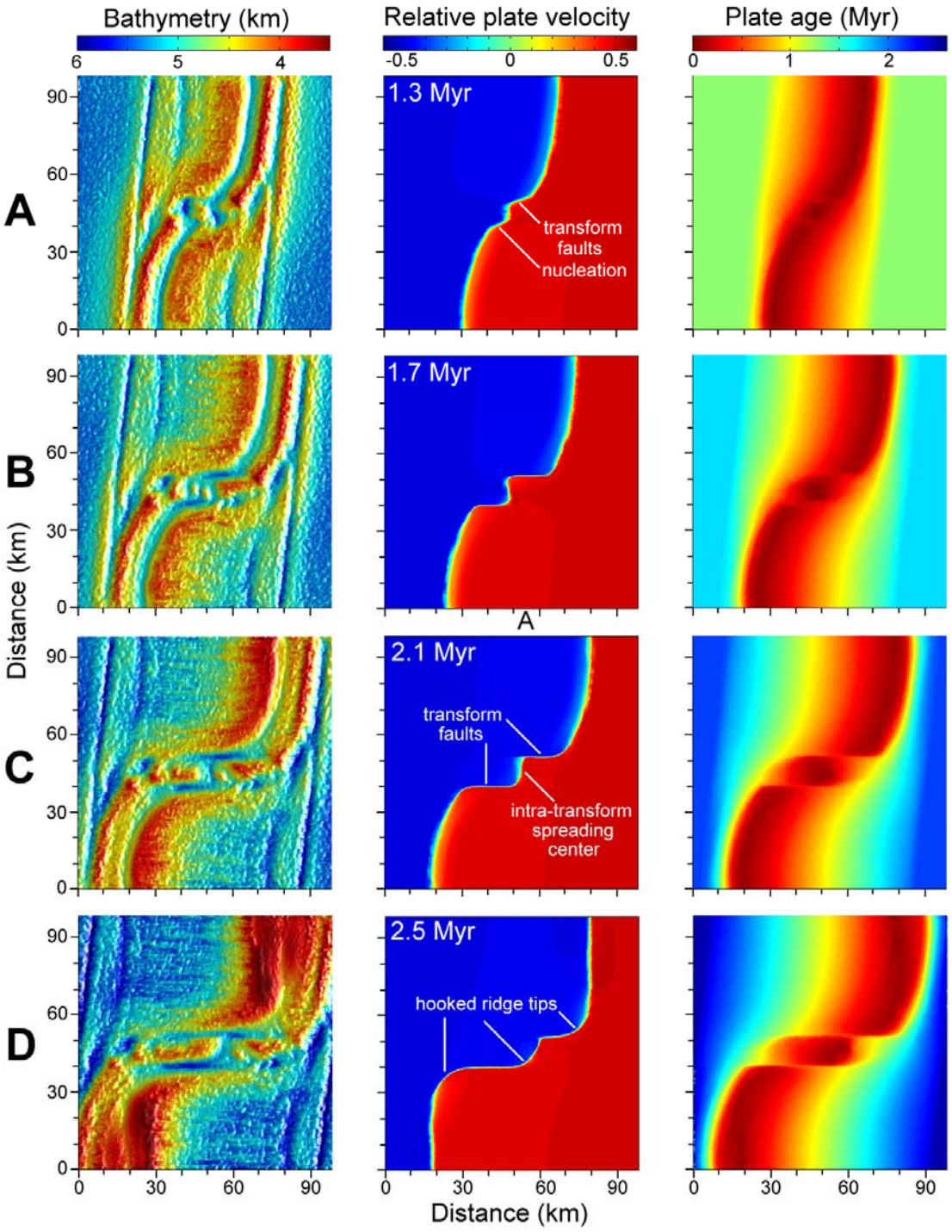

Figure S6. Development of transform faults associated with magmatic crust growth in case of initially inclined ridge (Model daij in Table S1, initial ridge inclination to z-axis is 11^{o}). Sea level for bathymetry maps (left column) is computed for every time step assuming constant (5 km) average depth of water above the growing crust. Note stabilization of ridge position after 2 Myr.

Table S1. Conditions and results of numerical experiments

Model	x-size (km)	z-size (km)	Spreading rate (cm/yr)	Thermal conductivity (W/m/K)	C_0/C_1 (MPa)	γ_0/γ_1	Plate viscosity (Pa s)	Mantle viscosity (Pa s)	Initial ridge inclination to z-axis	Fracture	results
dagsj	98	98	7.6	T-dependent*	60/1	0/1	10^{23}	10^{18}	0^o	wet	curved ridge, rotating blocks
dagsm	98	98	1.9	T-dependent*	100/1	0/1	10^{23}	10^{18}	0^o	wet	rotating blocks, transform faults
dagst	98	98	3.8	T-dependent*	30/1	0/1	10^{23}	10^{18}	0^o	wet	rotating blocks, transform faults
dagsu	98	98	3.8	T-dependent*	30/1	0/1	10^{22}	10^{18}	0^o	wet	curved ridge, orthogonal transform faults
dagsv	98	98	3.8	T-dependent*	30/1	0/1	10^{21}	10^{18}	0^o	wet	strongly curved ridge (zig-zag), inclined transform faults
dagsva	98	98	3.8	T-dependent*	30/1	0/1	$2x10^{21}$	10^{18}	0^o	wet	curved ridge, orthogonal transform faults
dagsw	98	98	3.8	T-dependent*	30/1	0/1	10^{20}	10^{18}	0^o	wet	viscous extension, no faults
dagsy	98	98	3.8	T-dependent*	60/30	0/1	10^{23}	10^{18}	3^o	wet	inclined ridge sections, rotating blocks
dagsz	98	98	3.8	T-dependent*	60/1	0/1	10^{23}	10^{18}	3^o	wet	rotating blocks, transform faults
dahe	98	98	3.8	T-dependent*	60/1	0/1	10^{23}	10^{18}	3^o	wet	rotating blocks, transform faults
dahf	98	98	3.8	T-dependent*	100/1	0/2	10^{23}	10^{18}	3^o	wet	rotating blocks, transform faults
dahg	98	98	3.8	T-dependent*	60/1	0.1/1.1	10^{23}	10^{18}	3^o	wet	rotating blocks, transform faults
dahh	98	98	3.8	T-dependent*	60/1	0.2/1.2	10^{23}	10^{18}	3^o	wet	curved ridge, orthogonal transform faults
dahha	98	98	3.8	T-dependent*	60/1	0.2/1.2	$3x10^{22}$	10^{18}	3^o	wet	ridge-parallel rolls, single transform fault
dahhb	98	98	3.8	T-dependent*	60/3	0.2/1.2	10^{23}	10^{18}	3^o	wet	rotating blocks, transform faults

dahhd	98	98	3.8	T-dependent*	60/1	0.2/2.2	10^{23}	10^{18}	3^{o}	wet	rotating blocks, transform faults
dahhe	98	98	3.8	T-dependent*	60/1	1/2	10^{23}	10^{18}	3^{o}	wet	gently inclined ridge with small offsets
dahhf	98	98	3.8	1	60/1	0.2/1.2	10^{23}	10^{18}	3^{o}	wet	curved ridge, small blocks
dahhg	98	98	3.8	2	60/1	0.2/1.2	10^{23}	10^{18}	3^{o}	wet	strongly curved ridge, orthogonal transform faults
dahhk	98	98	3.8	1.5	60/1	0.2/1.2	10^{23}	10^{18}	3^{o}	wet	curved ridge, rotating blocks
dahi	98	98	3.8	T-dependent*	60/1	0/0.5	10^{23}	10^{18}	3^{o}	wet	fragmented plates composed of small rotating blocks
dahj	98	98	3.8	T-dependent*	60/0.1	0/1	10^{23}	10^{18}	3^{o}	wet	curved ridge, rotating blocks
dahm	98	98	3.8	3	60/1	0/1	10^{23}	10^{18}	3^{o}	wet	two parallel ridges, ridge-parallel rolls, growth of a middle plate by accretion from two sides
dahn	98	98	3.8	T-dependent*	60/1	0/1	10^{23}	10^{18}	3^{o}	dry (no tensile fracture)	curved ridge, orthogonal and inclined transform faults
dahna	98	98	3.8	T-dependent*	60/1	0/1	10^{22}	10^{18}	3^{o}	dry (no tensile fracture)	curved ridge, asymmetric accretion
daho	98	196	3.8	T-dependent*	30/1	0/1	10^{22}	10^{18}	3^{o}	wet	curved ridge, orthogonal transform faults
dahq	98	98	3.8	T-dependent*	60/1	0/3	10^{23}	10^{18}	3^{o}	wet	gently curved ridge (zig-zag)
dahr	98	98	3.8	T-dependent*	60/1	0.5/1.5	10^{23}	10^{18}	3^{o}	wet	curved ridge, orthogonal transform faults
dahs	98	98	3.8	T-dependent*	60/10	0/1	10^{23}	10^{18}	3^{o}	wet	ridge-parallel rolls, rotating blocks
daht	98	98	3.8	T-dependent*	60/10	0.5/1.5	$5x10^{21}$	10^{18}	3^{o}	wet	curved ridge, orthogonal transform faults
dahu	98	98	3.8	3	60/10	0.5/1.5	10^{22}	10^{18}	3^{o}	wet	straight ridge, asymmetric accretion

dahua	98	98	3.8	1.5	60/10	0.5/1.5	10^{22}	10^{18}	3^{o}	wet	gently curved ridge (zig-zag)
dahv	196	98	3.8	T-dependent*	30/1	0.2/1.2	10^{22}	10^{18}	3^{o}	wet	curved ridge, orthogonal transform faults
dahw	196	98	3.8	T-dependent*	30/1	0.2/1.2	$3x10^{21}$	10^{18}	3^{o}	wet	curved ridge, asymmetric accretion
dahx	196	98	3.8	T-dependent*	30/1	0.2/1.2	$3x10^{22}$	10^{18}	3^{o}	wet	curved ridge, orthogonal transform faults
dahy	196	196	3.8	T-dependent*	30/1	0.2/1.2	10^{22}	10^{18}	0^{o}	wet	curved ridge, orthogonal transform faults
dahz	98	98	3.8	T-dependent*	30/1	0.2/1.2	10^{22}	10^{18}	0^{o}	wet	curved ridge, orthogonal transform faults
dahza	98	98	3.8	T-dependent*	30/3	0.2/1.2	10^{22}	10^{18}	0^{o}	wet	curved ridge, orthogonal transform faults
dahzb	98	98	3.8	2	30/1	0.2/1.2	10^{22}	10^{18}	0^{o}	wet	curved ridge, orthogonal transform faults
dahzc	98	98	3.8	T-dependent*	30/3	0.2/1.2	10^{22}	10^{18}	0^{o}	wet	rotating blocks, transform faults
dahzf	98	98	3.8	T-dependent*	30/10	0.2/1.2	10^{22}	10^{18}	0^{o}	wet	curved ridge, rotating blocks, asymmetric accretion
dahzg	98	98	3.8->7.6 (2->2.5 Myr)**	T-dependent*	30/3	0.2/1.2	10^{22}	10^{18}	0^{o}	wet	curved ridge, orthogonal transform faults, turn to single straight ridge in 6 Myr after plate velocity increase
dahzh	98	98	3.8	2	30/10	0.2/1.2	10^{22}	10^{18}	0^{o}	wet	curved ridge, rotating blocks, asymmetric accretion
dahzi***	98	98	3.8	T-dependent*	30/3	0.2/1.2	10^{22}	10^{18}	0^{o}	dry (no gravity)	curved ridge, orthogonal transform faults
dahzj	98	98	3.8->7.6 (1.5->2 Myr)**	T-dependent*	30/3	0.2/1.2	10^{22}	10^{18}	0^{o}	wet	curved ridge, orthogonal transform faults
dahzk	98	98	3.8->7.6 (2->2.5	T-dependent*	30/1	0.2/1.2	10^{22}	10^{18}	0^{o}	wet	gently curved ridge

			Myr)**								
dahzl	98	98	3.8	T-dependent*	30/3	0.2/1.2	10^{22}	10^{18}	0^{o}	dry	curved ridge, orthogonal transform faults
dahzn	98	98	3.8	T-dependent*	30/1	0.2/1.2	10^{22}	10^{18}	0^{o}	dry	curved ridge, inclined transform faults
dahzo	98	98	3.8	2	30/1	0.2/1.2	10^{22}	10^{18}	0^{o}	dry	curved ridge, orthogonal transform faults
dahzq	98	98	3.8	2	30/1	0.2/1.2	$3x10^{22}$	10^{18}	0^{o}	dry	curved ridge, orthogonal transform faults
dahzr	98	98	3.8	2	30/1	0.2/1.2	10^{23}	10^{18}	0^{o}	dry	curved ridge, orthogonal transform faults
dahzs	98	98	3.8	2	30/1	0.2/1.2	10^{22}	10^{19}	0^{o}	dry	Gently curved ridge with no transform faults (until 9 Myr)
dahzt	98	98	3.8	2	30/1	0.2/1.2	10^{22}	10^{20}	0^{o}	dry	ridge-parallel rolls, growth of a middle plate by accretion from two sides
dahzu	98	98	3.8	T-dependent*	30/3	0.2/1.2	10^{22}	10^{18}	0^{o}	wet	curved ridge, orthogonal transform faults
dahzv	98	98	3.8	T-dependent*	30/3	0.2/1.2	10^{22}	10^{18}	0^{o}	dry	curved ridge, orthogonal transform faults, asymmetric accretion
dahzw	98	98	3.8	T-dependent*	30/3	0.2/1.2	10^{22}	10^{19}	0^{o}	wet	curved ridge, inclined transform faults, asymmetric accretion
dahzx[$]	98	98	3.8	T-dependent*	30/3	0.2/1.2	10^{22}	10^{18}	0^{o}	wet	curved ridge, asymmetric accretion
dahzz	98	98	3.8	T-dependent*	30/3	0.2/1.2	10^{22}	10^{18}	0^{o}	wet	curved ridge, orthogonal transform faults
daia[$]	98	98	3.8	T-dependent*	30/3	0.2/1.2	10^{22}	10^{18}	27^{o}	wet	curved ridge, orthogonal transform fault
daic	98	98	3.8	T-dependent*	30/3	0.2/1.2	10^{22}	10^{18}	27^{o}	wet	curved ridge, orthogonal transform fault
daid	98	98	3.8	T-dependent*	30/3	0.2/1.2	10^{22}	10^{18}	11^{o}	wet	curved ridge, orthogonal transform faults, intra-transform spreading

											centers
daie	98	98	1.9	T-dependent*	30/3	0.2/1.2	10^{22}	10^{18}	27^{o}	wet	curved ridge, orthogonal transform fault
daif	98	98	1.9	T-dependent*	30/3	0.2/1.2	10^{22}	10^{18}	11^{o}	wet	curved ridge, orthogonal transform faults, rotating blocks
daig[$]	98	98	3.8	T-dependent*	30/3[&]	0.2/1.2	10^{22}	10^{18}	0^{o}	wet	curved ridge, orthogonal transform faults,
daii[$]	98	98	3.8	T-dependent*	30/3	0.2/1.2	10^{22}	10^{18}	27^{o}	wet	curved ridge, orthogonal transform fault
daij[$]	98	98	3.8	T-dependent*	30/3	0.2/1.2	10^{22}	10^{18}	11^{o}	wet	curved ridge, orthogonal transform faults, intra-transform spreading centers
daiz[$]	98	98	5.7	T-dependent*	30/3	0.2/1.2	10^{22}	10^{18}	11^{o}	wet	curved ridge, orthogonal transform faults, intra-transform spreading

* temperature-dependent thermal conductivity $0.73+1293/(T_K+77)$ (*23*)
** initial plate divergence velocity of 3.8 cm/yr was gradually increased to 7.6 cm/yr during the specified time period and then remained constant
*** no gravity in this model, pressure in the water layer is set to 50 MPa.
[$] magmatic growth of the oceanic crust is included to the model.
[&] lowered plastic strength of the oceanic crust (C_0=C_1=3 MPa)

References (supporting online material)

1. T. V. Gerya, D. A. Yuen, Phys. Earth Planet. Int. 163, 83 (2007).
2. T. V. Gerya, Introduction to Numerical Geodynamic Modelling (Cambridge University Press, Cambridge, 2010).
3. D.L. Turcotte, G. Schubert, Geodynamics (Cambridge University Press, Cambridge, 2002).
4. W. R. Buck, L. L. Lavier, A. N. B. Poliakov, Nature, 434, 719 (2005).
5. E. Choi, L. Lavier, M. Gurnis, Phys. Earth Planet. Interiors 171, 374 (2008).
6. C. F. Hieronymus, Earth Planet. Sci. Lett. 222, 177 (2006).
7. R. S. Huismans, C. Beaumont, Geology 30, 211 (2002).
8. A. Y. Rozhko, Y. Y. Podladchikov, F. Renard, Geophys. Res. Lett., 34, Article No. L22304 (2007)
9. S. A. F. Murrell, Br. J. Appl. Phys., 15, 1123 (1964).
10. J. C. Jaeger, J. Geophys. Res., 68, 6066 (1963).
11. J. Escartín, G. Hirth, B. Evans, Geology 29, 1023 (2001).
12. N. Hilairet, B. Reynard, Y. Wang, I. Daniel, S. Merkel, N. Nishiyama, S. Petitgirard, Science 318, 1910 (2007).
13. H. J. B. Dick, J. Lin, H. Schouten, Nature 426, 405 (2003).
14. K. A. Kriner, R. A. Pockalny, R. L. Larson, Earth Planet. Sci. Lett., 242, 98 (2006).
15. K. Nikolaeva, T. V. Gerya, J.A.D. Connolly, Phys. Earth Planet. Interiors, 171, 336 (2008).
16. M. M. Hirschmann, Geochem. Geophys. Geosyst., 1, Article No. 1042, (2000).
17. P.C. Hess, Origin of Igneous Rocks (Harward University Press, London, 1989).
18. J.A.D. Connolly, M.W. Schmidt, G. Solferino, N. Bagdassarov, Nature, 462, (2009).
19. P.M. Gregg, M.D. Behn, J. Lin, T.L. Grove, J. Geophys. Res., 114 Article No. B11102 (2009).
20. D. W.Oldenburg, J. N. Brune, Science 178, 301 (1972).
21. E. L. Winterer, in The Geophysics of the Pacific Ocean Basin and its Margin, G. H. Sutton, M.H. Manghnani, R. Moberly, Eds. (1976), pp. 269-280.
22. H. Schmeling et al., Phys. Earth Planet. Interiors 171, 198 (2008).
23. C. Clauser, E. Huenges, in Rock Physics and Phase Relations, T. J. Ahrens, Ed. (1995), pp. 105-126.